IEEE Access
Multidisciplinary ⋮ Rapid Review ⋮ Open Access Journal

Received March 10, 2020, accepted March 27, 2020, date of publication March 31, 2020, date of current version April 17, 2020.

Digital Object Identifier 10.1109/ACCESS.2020.2984733

An Application of Super-Resolution Generative Adversary Networks for Quasi-Static Ultrasound Strain Elastography: A Feasibility Study

LIANHAI HE[1], BO PENG[1,2,3], TIANLAN YANG[1], AND JINGFENG JIANG[4]

[1]School of Computer Science, Southwest Petroleum University, Chengdu 610500, China
[2]Department of Echocardiography and Noninvasive Cardiology, Sichuan Academy of Medical Science, Sichuan Provincial People's Hospital, Chengdu 610072, China
[3]Ultrasound in Cardiac Electrophysiology and Biomechanics Key Laboratory of Sichuan Province, Chengdu 610072, China
[4]Department of Biomedical Engineering, Michigan Technological University, Houghton, MI 49931, USA

Corresponding author: Bo Peng (bopeng@swpu.edu.cn)

This work was supported in part by the research grants from the Science and Technology Council of Chengdu under Grant 2019-GH02-00040-HZ, and in part by the Nanchong Scientific Council (Strategic Cooperation Program between University and City) under Grant NC17SY4020.

ABSTRACT In this work, a super-resolution approach based on generative adversary network (GAN) was used to interpolate (up-sample) ultrasound radio-frequency (RF) echo data along the lateral (perpendicular to the acoustic beam direction) direction before motion estimation. Our primary objective was to investigate the feasibility of using a GAN-based super-solution approach to improve lateral resolution in the RF data as a means of improving strain image quality in quasi-static ultrasound strain elastography (QUSE). Unlike natural scene photographs, axial (parallel to the acoustic beam direction) resolution is significantly higher than that of lateral resolution in ultrasound RF data. To better handle RF data, we first modified a super-resolution generative adversary network (SRGAN) model developed by the computer vision community. We named the modified SRGAN model as super-resolution radio-frequency neural network (SRRFNN) model. Our preliminary experiments showed that, compared with axial strain elastograms obtained using the original ultrasound RF data, axial strain elastograms using ultrasound RF data up-sampled by the proposed SRRFNN model were improved. Based on the Wilcoxon rank-sum tests, such improvements were statistically significant ($p < 0.05$) for large deformation (3-5%). Also, the proposed SRRFNN model outperformed a commonly-used method (*i.e.* bi-cubic interpolation used in MATLAB [Mathworks Inc., MA, USA]) in terms of improving axial strain elastograms. We concluded that applying the proposed (SRRFNN) model was feasible and good-quality strain elastography data could be obtained in *in vivo* tumor-bearing breast ultrasound data.

INDEX TERMS Generative adversarial network, motion tracking, super-resolution, quasi-static ultrasound strain elastography.

I. INTRODUCTION

Qusai-static ultrasound strain elastography (QUSE) [1], [2], which mimics manual palpation, has emerged as an useful imaging tool for non-invasive differentiation of breast and thyroid tumors [3]–[5], assessment of vascular plaques [6] and monitoring thermal ablation therapies [7], [8]. Recently, developments in QUSE shows potential in 3D breast and abdominal imaging [9]–[11]. In QUSE, first, one pre-compression ultrasound echo frame is acquired and then, tissues are deformed to acquire a post-compression ultrasound echo frame. Motion tracking is performed between the pair of pre- and post-compression echo frames to obtain ultrasonically-tracked tissue displacements. Finally, a strain elastogram representing spatial gradients of tissue displacements is formed to infer the hardness of tissues being imaged. Consequently, these ultrasonically-estimated displacements contain fundamental information and relentless efforts have been devoted to the improvement of displacement tracking accuracy.

The associate editor coordinating the review of this manuscript and approving it for publication was Gina Tourassi.

In the last few years, deep-learning neural network methods have gained rapid attention in many medical image applications [12]. Certainly, this trend has influenced technological developments in ultrasound elastography. Notably, neural network models [13], [14] have been tested as a part of QUSE's image reconstruction process. In the study by Gao *et al.* [13], a conventional neural network (CNN) model with prior information was directly used to produce strain images. Our group [14] retrained three well-known CNN models (FlowNet 2.0 [15], LiteFlowNet [16], PWC-Net [17]) developed in the computer vision community. Retraining enabled more reliable motion tracking for QUSE using ultrasound images. Both studies showed promising results and the future of using deep-learning neural network models in ultrasound elastography is bright. Particularly, the performance of the retrained PWC-Net model is on par with two well-known motion tracking algorithms [37], [50] used by QUSE.

Adversarial training can make CNN models more robust and improve the performance of CNN models. The adoption of adversarial training has led to developments of another type of neural network model known as generative adversary network (GAN) [18]. The use of GAN models has been extended into many ultrasound applications including speckle reduction [19], real-time ultrasound simulation [20], generation of multi-focused ultrasound image [21], novel beamforming [22] and B-mode image segmentation [23]. However, to our knowledge, GAN models have not been used for any ultrasound elastography modalities including QUSE.

As the first feasibility study, our primary objective is to investigate whether or not a GAN-based super-resolution model can be used to improve the lateral resolution of ultrasound data. As a result, we expect that strain image quality in QUSE can be improved when laterally-upsampled ultrasound data are used.

II. RELATED WORK AND OUR CONTRIBUTIONS

We are particularly interested in GAN-based super-solution methods because they showed superior performance over similar models based on convolution neural network (CNN) models and other machine-learning techniques. Interested readers are referred to two recent survey papers [24], [25] for detailed assessments. Ledig *et al.* [26] first proposed a GAN model named super-resolution GAN (SRGAN) to upscale natural scene images by a factor of 4. The performance of the SRGAN model was superior as compared to other state-of-the-art methods [26]. Wang *et al.* [27] further enhanced the SRGAN, which resulted in an enhanced SRGAN (ESRGAN) model. Enhancements proposed by Wang *et al.* were in the following three key areas: network architecture, adversarial loss, and perceptual loss. Due to improvements in those three major areas, ESRGAN consistently performed better than SRGAN [24], [25].

Now referring to motion tracking, a critically important step in QUSE, motion tracking methods are often applied to ultrasound radiofrequency (RF) data as opposed to ultrasound intensity images (*i.e.* B-mode) [28], [29]. However, the ESRGAN model [27] cannot be directly applied to ultrasound radiofrequency (RF) data. This is because RF data contain echo waveforms with significant amplitude variations and discrepancies between the axial and lateral resolution. Significant modification of the ESRGAN model as detailed in Section III enabled us to improve lateral resolution for ultrasound RF data. We named the proposed GAN-based super-resolution method to super-resolution radio-frequency neural network (SRRFNN) model.

To show benefits of using our SRRFNN model, elastographic results obtained by our SRRFNN model are compared to those obtained by a bi-cubic interpolator [44] (*i.e.* interp2 function in MATLAB [Mathworks Inc., MA, USA]) and without any lateral interpolations. The selection of bi-cubic interpolation in this feasibility study is largely due to a paucity of alternative interpolators commonly used in QUSE. Recall that the up-sampling of ultrasound data has not gained a lot of traction in QUSE. Hence, only a few studies were found in the literature. Konofagou and Ophir [30] applied a weighted interpolation scheme onto RF ultrasound data to improve lateral displacement tracking. Their interpolation scheme was mainly linear. Viola and Walker [31] used spline functions to represent ultrasound echo data so that the benefits of improving signal coherence can be gained without the actual up-sampling. More recently, Liu *et al.* [32] investigated how interpolations of RF data and correlation function along the lateral direction could influence motion tracking accuracy. Although they were interested in lateral displacement estimation, their results did suggest that up-sampling RF data along the lateral direction should have little effects on the axial motion tracking accuracy using Cosine interpolation. Given the fact that only conventional interpolation methods were used in the QUSE literature, our selection of bi-cubic interpolator as the baseline for comparison in the study seems appropriate.

The main contributions of this work are summarized as follows:

- Compared with the existing super-resolution GAN methods designed for photographic imagery, a modified GAN method named super-resolution radio-frequency neural network (SRRFNN) model is developed to improve lateral resolution of ultrasound RF data.
- Ultrasound data processed by a GAN-based super-resolution model are used for motion tracking for the first time. Neural network-based super-resolution techniques have not been applied to up-sample ultrasound echo data for ultrasound elastography applications, though a CNN-based model has been applied to B-mode images for better visualization [33]. Feasibility demonstrated by this work also opens a new avenue for applying GAN methods to other ultrasound elastography modalities such as shear wave elastography (SWE), acoustic radiation force imaging (ARFI). This is because motion tracking is a critically important step for QUSE,

SWE and ARFI. The definitions of QUSE, SWE and ARFI can be found in the consensus recommended by the World Federation of Ultrasound in Medicine and Biology [2].

The rest of this paper is organized as follows. Section III describes the SRRFNN model and related training. The modified ESRGAN model was applied to *in vivo* ultrasound data [3] acquired from 22 human subjects to demonstrate its ability to generate superior strain images. The highlight of Section IV is comparing strain images obtained using up-sampled ultrasound data by the modified GAN model to those obtained from up-sampled ultrasound data by a conventional bi-cubic interpolation method. Finally, Section V presents a summary discussion of our major findings and some limitations of the current study followed by a few closing remarks.

III. METHODS AND MATERIALS

A. A BRIEF DESCRIPTION OF PROPOSED SRRFNN MODEL

In the study, the original ESRGAN model was selected as our starting point because its known superior performance as reported by Wang *et al.* [27]. Modifications of its original architecture were conducted as described below so that the proposed SRRFNN model (see Fig. 1) can be used to upscale RF echo data along the lateral (perpendicular to the acoustic beam direction) direction for strain elastography applications.

In principle, the input to the generator G is a low-resolution RF (LR-RF) field and the output is a super-resolution RF (SR-RF) field. As shown in Fig. 1, the generator G is trained to produce an output SR-RF field that cannot be distinguished by the trained discriminator, D, which is trained to do its best in terms of detecting "faked" SR-RF fields.

The goal of the proposed SRRFNN model is to obtain a high-resolution, super-resolved two-dimensional (2D) RF field RF^{SR} from a low-resolution RF field (*i.e.* input RF^{LR}), which is the low-resolution version of its high-resolution counterpart RF^{HR}. Because RF^{HR} is only available during training, we use RF^{SR} to represent a computer-generated super-resolved RF field, which may differ from the true RF^{HR}. RF^{LR}, RF^{HR} and RF^{SR} are all real-value 2D matrices. The size of RF^{LR} is $W \times H$, while both RF^{HR} and RF^{SR} have identical size of $rW \times rH$, where r (> 1) is a positive integer and represent a pre-determined up-sampling factor.

Based on the original ESRGAN model proposed by Ledig *et al.* [26] and revised by Wang *et al.* [27], we redesigned the generator and discriminator networks (see Fig. 1). More details are provided below in proceeding Sections III-A1 and III-A2.

1) GENERATOR NETWORK

The proposed generator is a feed-forward CNN G_{θ_G} (Fig. 1) which takes a RF^{LR} as input and gives a RF^{SR} which is highly similar to the actual RF^{LR} as output. $\theta_G = \{W_1, B_1\}$ represents a collection of weights and biases of the CNN model because, mathematically, a convolution layer with biases can be described below,

$$F_1(X) = \begin{cases} W_1 \star X + B_1, & if\ W_1 \star X + B_1 > 0 \\ \alpha * (W_1 \star X + B_1), & if\ W_1 \star X + B_1 \leq 0 \end{cases} \quad (1)$$

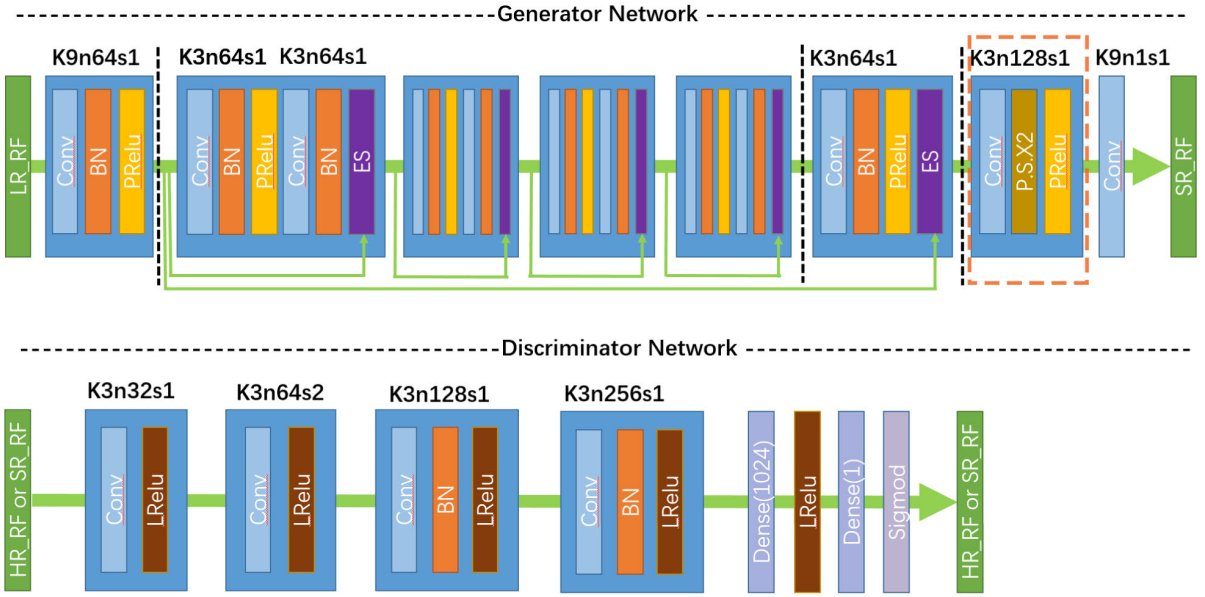

FIGURE 1. Architecture of Generator and Discriminator Networks with corresponding kernel size (k), number of feature maps (n) and stride (s) indicated for each convolutional layer. BN, PReLu, LReLu and ES stand for batch normalization [34], parametric ReLu activation function [35], leaky ReLu activation function and element-wise summation, respectively. Conv denotes a standard convolution operation. The upsampling in the generator network is done in layers contained in the dashed box.

where $\star$ represents a conventional convolution operation and α is a "learnable" parameter ranging from 1 to ∞.

G_{θ_G} has 4 components as shown in Fig. 1. Starting with a low-resolution RF (LR-RF) signal X, the first component contains a convolution layer with 9×9 kernels and 64 feature maps followed by batch-normalization (BN) layers and Parametric ReLU (PReLu) [35] as the activation function. The stride size is 1.

The second component has four residuals blocks; each block consists of two convolution layers with smaller 3×3 kernels and 64 feature maps followed by BN layers, PReLu units as the activation function and element-wise summations (ES). Jump connections are used in the second component to connect the input and output characteristics of each residual block. The second component is named as residual networks/blocks because of the presence of jump connections, which are often used to solve vanishing gradients [36] to mitigate difficulty during training.

The third component is similar to the second component except for the following differences. First, there is only one convolution layer following by BN layers, PReLU units and ESs. Second, jump connections are not included.

The fourth component consists of two convolution layers and a pixel shuffle layer. More detailed parameters regarding kernel size, number of feature maps and stride are shown in Fig. 1. Of note, the pixel shuffle layer performs convolution at $1/r$ pixel scale (r is the up-sample factor mentioned above) and therefore can increase the size of the feature maps without interpolation. The generator network outputs a super-resolution RF signal with increased lateral resolution and leaves axial resolution unchanged.

In order to train N super-resolved RF fields RF_n^{SR}, $n = 1, 2, \ldots, N$ that are highly similar to known ground truth (*i.e.* N known high-resolution RF fields RF_n^{HR}, $n = 1, 2, \ldots, N$), we use N low-resolution RF fields ($RF_n^{LR}, n = 1, 2, \ldots, N$) as input to minimize the following energy function:

$$\hat{\theta}_G = \arg\min_{\theta_G} \frac{1}{N} \sum_{n=1}^{N} l^{SR}\{G_{\theta_G}(RF_n^{LR}), RF_n^{HR}\} \tag{2}$$

where l^{SR} is a loss function described below and $G_{\theta_G}(RF_n^{LR})$ denotes a super-resolved RF field produced by the generator network.

In this study, a spatial continuity term C has been added to the loss function l^{SR} as follows,

$$\begin{aligned} l^{SR} &= -\log\{D_{\theta_D}(G_{\theta_G}(RF_n^{LR}))\} \\ &\quad + 0.1 \times \frac{1}{rWH} \sum_{x=1}^{rW} \sum_{y=1}^{H} (|RF_{x,y}^{HR} - G_{\theta_G}(RF_{x,y}^{LR})|) \\ &\quad + 2. \times 10^{-8} C \end{aligned} \tag{3a}$$

$$C = \sum_{x=1}^{rW} \sum_{y=1}^{H} \{G_{\theta_G}(RF^{LR})_{x,y-1} - G_{\theta_G}(RF^{LR})_{x,y}\}^2 + \sum_{x=1}^{rW} \sum_{y=1}^{H} \{G_{\theta_G}(RF^{LR})_{x+1,y} - G_{\theta_G}(RF^{LR})_{x,y}\}^2 \tag{3b}$$

where log is a natural log function, θ_D is a collection of parameters associated with the proposed discriminator network (Section III-A2), and $D_{\theta_D}(G_{\theta_G}(RF_n^{LR}))$ stands for the output from the discriminator network by taking a super-resolved RF field generated by the generator network as the input. In Eqns. (3a) and (3b), x and y are coordinates, and the weight (0.1) was empirically chosen to balance contributions from three terms to the overall loss.

2) DISCRIMINATOR NETWORK

The discriminator network D_{θ_D} consists of 4 convolution layers and 2 fully connected layers. The sigmoid function is adopted as the activation function. The discriminating network is used to determine whether or not the input RF^{SR} signal produced by the generator network (see Section III-A1) is a real RF^{HR} signal.

3) OVERALL LOSS FUNCTION

The overall loss function for the proposed SRRFNN model is written as follows:

$$\begin{aligned} L(G, D) &= \mathbb{E}_{RF^{HR} \sim P_{training}(RF^{HR})}[\log(D_{\theta_D}(RF^{HR}))] \\ &\quad + \mathbb{E}_{RF^{LR} \sim P_G(RF^{LR})}[\log(1 - D_{\theta_D}(G_{\theta_G}(RF^{LR})))] \end{aligned} \tag{4}$$

where RF^{LR} and RF^{HR} denote the low-resolution and high-resolution RF signals, respectively, $G_{\theta_G}(RF^{LR})$ represents super-resolution RF signals generated by the generator and $D_{\theta_D}(G_{\theta_G}(RF^{LR}))$ is the output of the discriminator network, which represents its assessment of the super-resolution RF signal by the generator.

B. TRAINING OF THE PROPOSED SRRFNN MODEL

The training of SRRFNN (see Fig. 1) was to achieve an optimal network $\widehat{G}$ by solving the following min-max problem as first developed by Goodfellow *et al.* [18]:

$$\widehat{G} = \arg\min_{\theta_G} \max_{\theta_D} L(G, D) \tag{5}$$

More specifically, the entire training process was done by alternating the training of both the generator (Eqn. 2) and discriminator (Eqn. 5) networks. *In vivo* RF ultrasound data acquired from human subjects were used to train.

From our internal database, ultrasound data acquired from 50 human subjects with pathologically-confirmed breast lesions were arbitrarily selected. Ultrasound data from each patients contain 50-90 frames. All *in vivo* ultrasound data were acquired using a Siemens Elegra scanner equipped with a high frequency linear array transducer (7.5 MHz, Siemens Medical Solution (USA) Inc., CA, USA). Axial sample spacing and lateral line spacing were 0.021 mm and 0.19 mm, respectively. The detailed protocol for data acquisition was previously reported by Hall *et al.* [3]. All data acquisition was

approved by appropriate oversight institutional review boards (IRBs) and patient consents were obtained.

1130 RF frames randomly selected from 28 human subjects (among 50 human subjects) were pre-processed before being used for training. In the first pre-processing step, the lateral resolution of those RF frames was interpolated up by a factor 10 using bi-cubic interpolation method. After this up-sampling, one RF frame contains 1920 × 2000 samples. In the second pre-processing step, the interpolated ultrasound data were divided into smaller patches (200 × 200 samples). Thus, each RF field can produce 50 non-overlapping patches. Those 200 × 200 patches are used as high-resolution RF (*i.e.* $HR - RF$) and their down-sampled versions (200 × 100) are used as low-resolution RF (*i.e.* $LR - RF$). In the last pre-processing step, all data were normalized between -1 and 1.

Totally, we obtained 56,500 patches after all pre-processing steps mentioned above. Among them, 53,709 and 2,791 patches were used for training and validation, respectively.

The SRRFNN was trained on a computer workstation equipped with dual Intel CPUs (E2650, Intel, CA, USA) and a Graphic Processing Unit (GPU) card (TITAN, Nividia Inc., CA, USA). The implementation was done under the well-known open-source PyTorch framework[1] and Adam optimizer was used to perform the training with the following parameters: up-sampling factor $r = 2$, $\beta_1 = 0.5$, $\beta_2 = 0.999$, batch size=16, and initial learning rate =0.0002.

C. EVALUATION OF THE PROPOSED UP-SAMPLING STRATEGY

After the completion of up-sampling of RF data, motion tracking was performed on those up-sampled RF data using a GPU-accelerated coupled speckle tracking algorithm [9], [37]. The tracking kernel size is approximately 2.1 mm (6 wavelengths long along the axial direction) × 1 mm (approximately 1 beam width along the lateral direction). More details of the motion tracking algorithm can be found in our prior publications [9], [37]. In order to demonstrate the effect of using the proposed SRRFNN model, motion tracking using the above-mentioned GPU-accelerated coupled algorithm was also performed on original RF data and (2X) up-sampled RF data using a bi-cubic interpolator [44].

Using a single-inclusion two-dimensional (2D) numerical phantom (40 mm × 40 mm; plane stress condition) in the first test, displacement estimation was performed at 7 deformation levels (0.1%, 0.5%, 1%, 2%, 3%, 4% and 5%) to obtain displacements at a 200 × 200 grid. The simulated inclusion was 5 times stiffer than its background. Computer-simulated ultrasound data were created using the combination of finite element (FE; ANSYS Inc., PA, USA) and Field II ultrasound simulations [38], [39]. Field II simulations were done to mimic a 7.5 MHz linear array transducer. Then, estimated displacements were decimated by a factor of 5 in each dimension to reduce statistical dependence. The remaining 1600 displacement estimates were used to calculate tracking errors along the axial and lateral directions as follows:

$$Error_{a,l} = disp_t - disp_e \tag{6}$$

where $disp_t$ and $disp_e$ are true and estimated displacements, respectively. In Eqn. (6), subscripts a and l stand for axial and lateral directions, respectively. Error variances were calculated at each deformation level to assess motion tracking accuracy.

After a displacement field had been obtained, local strains were calculated by using a low-pass strain estimation method [40]. All strain elastograms were formed on an isotropic grid of 0.2 mm. In addition to visual evaluations, area-weighted contrast-to-noise ratio (CNR) was used to assess the quality of strain elastograms [41]:

$$CNR = \frac{|I_t - I_b|}{\sqrt{w_t {\sigma_t}^2 + w_b {\sigma_b}^2}} \tag{7}$$

where I and σ denote means and variances of signals, and subscripts b and t represent the background and target, respectively. The CNR (Eqn. (7)) is weighted by areas of the background w_b and the target w_t, respectively. Manual image segmentation was perform for each strain elastogram to differentiate the target from the rest of the strain image, referred to hereafter as the background. All manual lesion segmentation tasks were done by an engineer who has approximately 10-year experience in SE including algorithm development and image analysis. Eqn. (7) was adopted to account for the fact that the background and target usually have different numbers of pixels. Song *et al.* [41] demonstrated that consideration of the weighted area is necessary in such a situation.

In the second test, remaining twenty-two (22) data sets from the above-mentioned 50 selected human subjects were used for testing. Thus, our training and testing ultrasound data sets have no overlap.

Axial and lateral strain elastograms were reconstructed and CNR values were calculated using Eqn. (7) for all *in vivo* ultrasound data. In this study, we also investigated the performance of the proposed SRRFNN model under varying deformation (1% to 5%). In order to track large tissue deformation (3-5%), motion tracking was first performed at the level of (roughly) 1% frame-to-frame and then, a multiple-compression technique [37], [42], [43] was used to accumulate axial and lateral displacements/strains to reach 3-5% large deformation using the GPU-accelerated coupled tracking method.

All data analyses were performed using the computer workstation mentioned above for training of the proposed SRRFNN model.

IV. RESULTS

A. NUMERICAL PHANTOM RESULTS

By comparing ultrasonically-tracked displacements to FEA-simulated displacements (*i.e.* the ground truth in this case; see Eqn. (6)), error variances were obtained and are plotted in Figs. 2a-b. Fig. 2. Generally, both the proposed

[1] www.pytorch.org

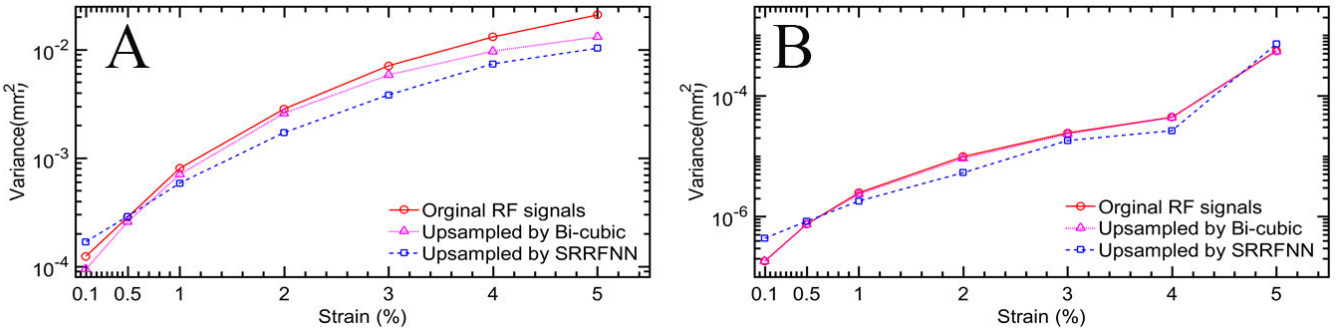

FIGURE 2. Comparisons of error variances for (a) lateral and (b) axial displacements at different axial compressions (0.1%-5%).

SRRFNN model and the bi-cubic interpolation approach improved motion tracking as compared to motion tracking performed on the original ultrasound RF data. The improvements were greater by using the SRRFNN model than those obtained by the bi-cubic interpolation approach except at the small deformation (*i.e.* $< 0.5\%$)

We also estimated CNR values by using the computer-simulated single-inclusion phantom from 0.1-5% compression. Those estimated CNR values are shown in Fig. 3. Clearly, CNR values obtained from axial strain images were improved when the proposed SRRFNN model was used to up-sample RF data. The bi-cubic interpolation approach did not improve axial CNR values. However, the proposed SRRFNN model yielded slightly reduced CNR values obtained from lateral strain elastograms, though all lateral CNR values were low (see Fig. 3).

B. IN VIVO RESULTS

One representative example of tracking results (axial and lateral displacements, and axial and lateral strains) obtained from a breast invasive ductal carcinoma (IDC) is shown in Fig. 4. Visually, large motion tracking errors exist when original RF data or up-sampled RF data using the bi-cubic interpolation method are used (see arrows in Fig. 4a and b). However, no large tracking errors are visible in the axial displacements obtained using up-sampled RF data using the proposed SRRFNN model (Fig. 4b). That explains why the corresponding axial strain elastogram obtained using up-sampled RF data using the proposed SRRFNN model is smoother, as compared to its counterparts.

In another IDC example shown in Fig. 5, there are no large tracking errors for any of the three methods. However, using up-sampled RF data by the proposed SRRFNN model resulted in a ''cleaner'' axial strain elastogram. We observed that lateral displacements and strains were not improved. Particularly, the correspondence between axial and lateral displacement images was not improved and the IDC contours were not visible for any of three methods. As a result, the IDC cannot be seen from the lateral strain elastograms generated using original and upsampled RF data.

CNR values of axial and lateral strain elastograms (Fig. 6) were calculated. Both up-sampling methods did not improve the quality of lateral strain elastograms as shown in Fig. 6a. However, using upsampled RF data by the proposed SRRFNN model improved CNR values obtained from axial strain elastograms, as compared to results using up-sampled RF data via the bi-cubic interpolation method and original ultrasound data. Particularly, CNR values of axial strain elastograms using ultrasound RF data up-sampled by the proposed SRRFNN model were improved as compared to those obtained using original ultrasound data (see Fig. 6b). Based on Wilcoxon rank-sum tests, such improvements in terms of CNR values were statistically significant ($p < 0.05$) for large deformation (3-5%) as shown in Table 1. Furthermore, the

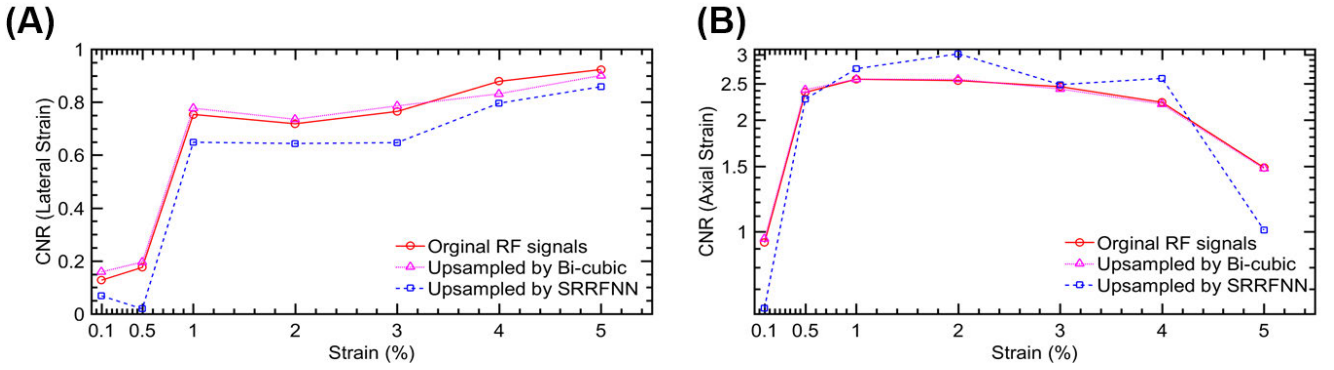

FIGURE 3. A plot showing calculated CNRs with respect to varying deformation levels from 0.1-5.0%. The CNR values were calculated from the single-inclusion numerical phantom whose error variances are displayed in Fig. 2.

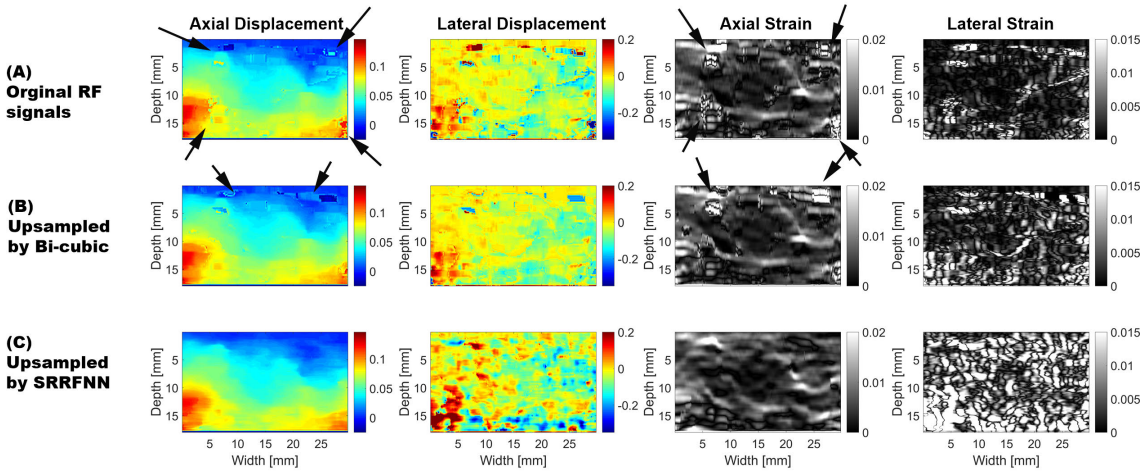

FIGURE 4. Resultant images obtained from up-sampled RF echo data using (a) original RF data without any interpolation (b) bicubic-interpolation and (c) the proposed SRRFNN model. Ultrasound RF data were acquired from a human subject containing an IDC. All axial and lateral displacement images are in mm. The frame-average axial strain is approximately 1%.

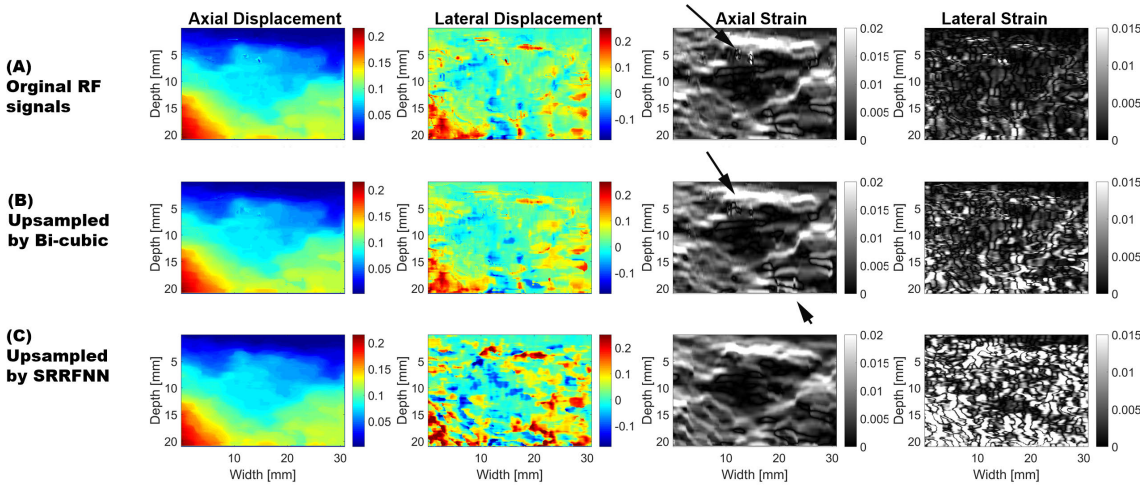

FIGURE 5. Resultant images obtained from up-sampled RF echo data using (a) original RF data without any interpolation (b) bicubic-interpolation and (c) the proposed SRRFNN model. Ultrasound RF data were acquired from a human subject containing another IDC. All axial and lateral displacement images are in mm. The frame-average axial strain is approximately 1%.

trend of gaining statistical significance from low compression to high compression is clearly seen in Table 1. In contrast, using RF data up-sampled by the bi-cubic interpolation approach did not improve the CNR values estimated from any of the axial strain elastograms based on Wilcoxon rank-sum tests.

V. DISCUSSION AND SUMMARY

In this paper, we applied the proposed SRRFNN model to up-sample RF data along the lateral direction and subsequently, used those up-sampled RF data to track motion and form strain images. To the best of our knowledge, this is the first study of this kind, in which a neural network-based up-sampling strategy was compared to bi-cubic interpolation for elastographic applications. The bi-cubic interpolation was a convolution-based interpolation algorithm [44] and our results remain unchanged if a bi-cubic spline interpolator is used.

Given the data investigated, we found that using the proposed SRRFNN model to up-sample ultrasound data along the lateral direction can improve axial motion tracking accuracy and therefore lead to better axial strain elastograms. When the bi-cubic interpolation along the lateral direction was used, our results were comparable to those reported by Liu *et al.* [32].

As shown in Fig. 1, the generator network is indeed a CNN model that first uses a series of convolution operations to extract features and then upsamples all extract features to a high-resolution ''image'' by a pixel shuffle layer (see the dashed box in Fig. 1). We stipulate that convolution operations remove noise contained in the image data and that will benefit subsequent motion tracking. We think this stipulation

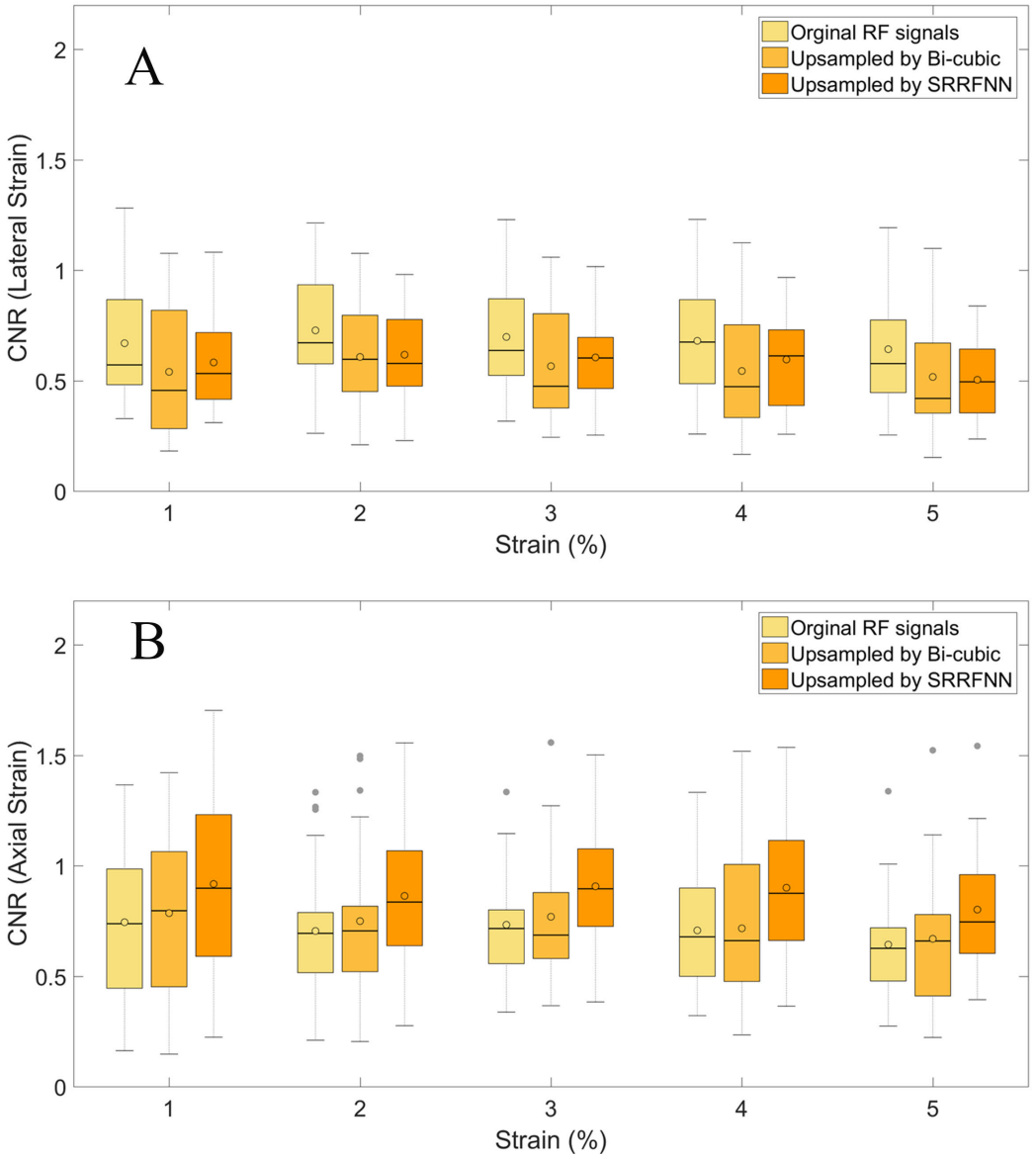

FIGURE 6. Clustered box-plot charts of CNR values obtained from 22 *in vivo* (a) lateral and (b) axial strain elastograms. The top and bottom of the boxes indicate 75 and 25 percentiles, respectively. The line and hollow circle through the middle of each box represent the median and the average, respectively. The error bars show the minimum and maximum values. Solid dots are outliers. RF ultrasound data were originally acquired from 22 human subjects with biologically-confirmed breast tumors. Those ultrasound data were upsampled using a bi-cubic interpolation method and the proposed SRRFNN model. P-values comparing CNN values among three groups can be found in Table 1.

TABLE 1. A summary of p-values obtained by comparing CNR values of axial and lateral strain elastograms from three groups: Original, Bicubic Sampling and SRRFNN as shown in Figs. 6a-b. The red fonts denote statistical significance ($p < 0.05$) has been achieved.

Compression	Lateral Strain (Fig. 6a)			Axial Strain (Fig. 6b)		
	Original vs. SRRFNN	*Original vs. Bicubic*	*Bicubic vs. SRRFNN*	*Original vs. SRRFNN*	*Original vs. Bicubic*	*Bicubic vs. SRRFNN*
1%	0.489	0.073	0.245	0.149	0.751	0.265
2%	0.108	0.162	0.860	0.108	0.614	0.185
3%	0.286	0.042	0.366	0.034	0.664	0.089
4%	0.275	0.103	0.330	0.024	0.897	0.053
5%	0.08	0.089	0.716	0.040	0.751	0.093

is reasonable for two reasons. **First**, convolution operations result in "local smoothing" of imaging data and this aspect is known in image processing field. We used *in vivo* RF data acquired from standard clinical scanners to train the proposed SRRFNN model. When we applied the trained SRRFNN model by *in vivo* RF data to computer-simulated RF data.

Motion tracking using simulated RF data interpolated by the proposed SRRFNN model yielded better results, as compared to those obtained by using un-interpolated simulated data and simulated data interpolated by a bic-cubic method (see Fig. 2). The improved NCC values are implicit indications of ''local smoothing''. **Second**, we also found supportive results in the literature. For instance, in a noise-removing CNN model [45] reported by Ding *et al.*, they started with a published super-resolution CNN model [46] and then replaced the last upsampling deconvolution layer in the super-solution CNN model with a dimension-enlargement layer without upsampling capabilities. Their new noise-removing CNN model was able to remove noise without upsampling. In short, we think the generator network inherited noise-removing capabilities intrinsic to CNN models.

In the literature, motion tracking in QUSE has been performed either on the raw RF/B-mode data [47]–[51] or features extracted from B-mode data [14], [52]. Motion tracking in this study was performed on upsampled features extracted from RF data using a CNN model. Hence, our approach could be considered as an alternative to existing methods.

Improvements shown in this study appeared to be subtle (See Figs. 4 and 5). One might think that regularized tracking algorithms [48]–[51] can also be effectively used to remove those tracking errors. This is certainly a valid point. However, the proposed approach offers an alternative. Although impressive regularized tracking algorithms [50], [51] from Prof. Rivaz's group have demonstrated that high-quality strain images can be obtained, regularized motion tracking in general could lead to biased tracking results. Visibly pleasing but biased displacements may pose challenges to modulus inversion algorithms [53]–[55]. Now, since the feasibility has been established, we expect that better results can be achieved by further optimizing the proposed SRRFNN model. In the future, we plan to do more testing our method, particularly using modulus inversion algorithms. This is because the quality of displacements is critically important for the success of modulus inversion and the outcome of modulus inversion is likely sensitive to the displacement quality when there is no regularization or weak regularization [53].

Lastly, in this study, our goal was to verify the performance of improving motion estimation by using the up-sampling of RF data along the lateral direction. During the training of the proposed SRRFNN model, the up-sampled *in vivo* RF signals were treated as the gold standard. When we applied the trained SRRFNN model to computer simulated data, the improvements measured by NCC values (Fig. 2) could be sub-optimal because the SRRFNN model was not trained using similar data. Overall, our training should still be considered as appropriate for this feasibility study.

In the future, we should consider the true ''high-resolution'' ultrasound data, *e.g.* high-frequency ultrasound data using novel beam-forming technology for training. Given the availability of an advanced ultrasound elastography simulation platform [38], [39], computer-simulated but realistic data of this kind can be used for training purposes. Now we have a better understanding the relationship between CNN-based super-resolution and noise removal [45], novel CNN models can be designed to improve the generator network accordingly.

In summary, we compared the displacements and strains obtained by two up-sampling strategies: (1) bi-cubic interpolation approach and (2) the proposed SRRFNN model. The elastographic results obtained using the original ultrasound data were used as a baseline in this study. We found that using laterally up-sampled RF data by the proposed SRRFNN model improved the tracking accuracy by a greater rate, as compared to the bi-cubic interpolation method. The mean CNR values of axial strain using bicubic-interpolated RF signals and the proposed SRRFNN model among 22 *in vivo* cases were 0.79 [bicubic] and 0.92 [the proposed] at 1% frame-average compression, respectively. If the original ultrasound RF data were used, the mean CNR value of axial strain elastograms at 1% frame-average compression was 0.72. Such improvement was consistent from 1-5% and reached statistical significance when the compression exceeded 2% (See Table 1). Improved motion tracking accuracy at large compression is important to nonlinear QUSE [56], particularly nonlinear modulus inversion [55].

ACKNOWLEDGMENT

The authors would like to thank Prof. Timothy Hall from the University of Wisconsin for providing them ultrasound data used in this study.

REFERENCES

[1] J. Ophir, ''Elastography: A quantitative method for imaging the elasticity of biological tissues,'' *Ultrason. Imag.*, vol. 13, no. 2, pp. 111–134, Apr. 1991.

[2] T. Shiina *et al.*, ''WFUMB guidelines and recommendations for clinical use of ultrasound elastography: Part 1: Basic principles and terminology,'' *Ultrasound Med. Biol.*, vol. 41, no. 5, pp. 1126–1147, May 2015.

[3] T. J. Hall, Y. Zhu, and C. S. Spalding, ''*In vivo* real-time freehand palpation imaging,'' *Ultrasound Med. Biol.*, vol. 29, no. 3, pp. 427–435, Mar. 2003.

[4] A. Lyshchik, T. Higashi, R. Asato, S. Tanaka, J. Ito, J. J. Mai, C. Pellot-Barakat, M. F. Insana, A. B. Brill, T. Saga, M. Hiraoka, and K. Togashi, ''Thyroid gland tumor diagnosis at US elastography,'' *Radiology*, vol. 237, no. 1, pp. 202–211, Oct. 2005.

[5] E. S. Burnside, T. J. Hall, A. M. Sommer, G. K. Hesley, G. A. Sisney, W. E. Svensson, J. P. Fine, J. Jiang, and N. J. Hangiandreou, ''Differentiating benign from malignant solid breast masses with US strain imaging,'' *Radiology*, vol. 245, no. 2, pp. 401–410, 2007.

[6] C. Huang, X. Pan, Q. He, M. Huang, L. Huang, X. Zhao, C. Yuan, J. Bai, and J. Luo, ''Ultrasound-based carotid elastography for detection of vulnerable atherosclerotic plaques validated by magnetic resonance imaging,'' *Ultrasound Med. Biol.*, vol. 42, no. 2, pp. 365–377, Feb. 2016.

[7] R. Righetti, F. Kallel, R. J. Stafford, R. E. Price, T. A. Krouskop, J. D. Hazle, and J. Ophir, ''Elastographic characterization of HIFU-induced lesions in canine livers,'' *Ultrasound Med. Biol.*, vol. 25, no. 7, pp. 1099–1113, Sep. 1999.

[8] J. Jiang, C. Brace, A. Andreano, R. J. DeWall, N. Rubert, T. G. Fisher, T. Varghese, F. Lee, and T. J. Hall, ''Ultrasound-based relative elastic modulus imaging for visualizing thermal ablation zones in a porcine model,'' *Phys. Med. Biol.*, vol. 55, no. 8, pp. 2281–2306, Apr. 2010.

[9] B. Peng, Y. Wang, T. J. Hall, and J. Jiang, ''A GPU-accelerated 3-D coupled subsample estimation algorithm for volumetric breast strain elastography,'' *IEEE Trans. Ultrason., Ferroelectr., Freq. Control*, vol. 64, no. 4, pp. 694–705, Apr. 2017.

[10] C. Papadacci, E. A. Bunting, and E. E. Konofagou, "3D quasi-static ultrasound elastography with plane wave *in vivo*," *IEEE Trans. Med. Imag.*, vol. 36, no. 2, pp. 357–365, Feb. 2017.
[11] Y. Wang, M. Bayer, J. Jiang, and T. J. Hall, "Large-strain 3-D *in vivo* breast ultrasound strain elastography using a multi-compression strategy and a whole-breast scanning system," *Ultrasound Med. Biol.*, vol. 45, no. 12, pp. 3145–3159, Dec. 2019.
[12] X. Yi, E. Walia, and P. Babyn, "Generative adversarial network in medical imaging: A review," *Med. Image Anal.*, vol. 58, Dec. 2019, Art. no. 101552.
[13] Z. Gao, S. Wu, Z. Liu, J. Luo, H. Zhang, M. Gong, and S. Li, "Learning the implicit strain reconstruction in ultrasound elastography using privileged information," *Med. Image Anal.*, vol. 58, Dec. 2019, Art. no. 101534.
[14] B. Peng, Y. Xian, Q. Zhang, and J. Jiang, "Neural-network-based motion tracking for breast ultrasound strain elastography: An initial assessment of performance and feasibility," *Ultrason. Imag.*, vol. 42, no. 2, pp. 74–91, 2020.
[15] E. Ilg, N. Mayer, T. Saikia, M. Keuper, A. Dosovitskiy, and T. Brox, "FlowNet 2.0: Evolution of optical flow estimation with deep networks," in *Proc. IEEE Conf. Comput. Vis. Pattern Recognit. (CVPR)*, Jul. 2017, pp. 2462–2470.
[16] T.-W. Hui, X. Tang, and C. C. Loy, "LiteFlowNet: A lightweight convolutional neural network for optical flow estimation," in *Proc. IEEE/CVF Conf. Comput. Vis. Pattern Recognit.*, Jun. 2018, pp. 8981–8989.
[17] D. Sun, X. Yang, M.-Y. Liu, and J. Kautz, "PWC-Net: CNNs for optical flow using pyramid, warping, and cost volume," in *Proc. IEEE Conf. Comput. Vis. Pattern Recognit. (CVPR)*, Jun. 2018, pp. 8934–8943.
[18] I. Goodfellow, J. Pouget-Abadie, M. Mirza, B. Xu, D. Warde-Farley, S. Ozair, A. Courville, and Y. Bengio, "Generative adversarial nets," in *Proc. Adv. Neural Inf. Process. Syst. (NIPS)*, Z. Ghahramani, M. Welling, C. Cortes, N. D. Lawrence, and K. Q. Weinberger, Eds. Montréal, QC, Canada: Curran Associates, 2014, pp. 2672–2680.
[19] F. Dietrichson, E. Smistad, A. Ostvik, and L. Lovstakken, "Ultrasound speckle reduction using generative adversial networks," in *Proc. IEEE Int. Ultrason. Symp. (IUS)*, Oct. 2018, pp. 1–4.
[20] B. Peng, X. Huang, S. Wang, and J. Jiang, "A real-time medical ultrasound simulator based on a generative adversarial network model," in *Proc. IEEE Int. Conf. Image Process. (ICIP)*, Sep. 2019, pp. 4629–4633.
[21] S. Goudarzi, A. Asif, and H. Rivaz, "Multi-focus ultrasound imaging using generative adversarial networks," in *Proc. IEEE 16th Int. Symp. Biomed. Imag. (ISBI)*, Apr. 2019, pp. 1118–1121.
[22] X. Zhang, J. Li, Q. He, H. Zhang, and J. Luo, "High-quality reconstruction of plane-wave imaging using generative adversarial network," in *Proc. IEEE Int. Ultrason. Symp. (IUS)*, Oct. 2018, pp. 1–4.
[23] A. A. Nair, T. D. Tran, A. Reiter, and M. A. L. Bell, "A generative adversarial neural network for beamforming ultrasound images : Invited presentation," in *Proc. 53rd Annu. Conf. Inf. Sci. Syst. (CISS)*, Mar. 2019, pp. 1–6.
[24] V. K. Ha, J. Ren, X. Xu, S. Zhao, G. Xie, and V. M. Vargas, "Deep learning based single image super-resolution: A survey," in *Advances in Brain Inspired Cognitive Systems*, J. Ren, A. Hussain, J. Zheng, C.-L. Liu, B. Luo, H. Zhao, and X. Zhao, Eds. Cham: Springer, 2018, pp. 106–119.
[25] W. Yang, X. Zhang, Y. Tian, W. Wang, J.-H. Xue, and Q. Liao, "Deep learning for single image super-resolution: A brief review," *IEEE Trans. Multimedia*, vol. 21, no. 12, pp. 3106–3121, Dec. 2019.
[26] C. Ledig, L. Theis, F. Huszar, J. Caballero, A. Cunningham, A. Acosta, A. Aitken, A. Tejani, J. Totz, Z. Wang, and W. Shi, "Photo-realistic single image super-resolution using a generative adversarial network," in *Proc. IEEE Conf. Comput. Vis. Pattern Recognit. (CVPR)*, Jul. 2017, pp. 105–114.
[27] X. Wang, K. Yu, S. Wu, J. Gu, Y. Liu, C. Dong, Y. Qiao, and C. C. Loy, "ESRGAN: Enhanced super-resolution generative adversarial networks," in *Proc. Eur. Conf. Comput. Vis.*, L. Leal-Taixé and S. Roth, Eds. Munich, Germany: Springer, 2018, pp. 63–79.
[28] M. M. Sette, P. Goethals, J. D'hooge, H. V. Brussel, and J. V. Sloten, "Algorithms for ultrasound elastography: A survey," *Comput. Methods Biomechanics Biomed. Eng.*, vol. 14, no. 3, pp. 283–292, 2011.
[29] J. Jiang and B. Peng, *Ultrasonic Methods for Assessment of Tissue Motion in Elastography*. Hoboken, NJ, USA: Wiley, 2018, ch. 4, pp. 35–70.
[30] E. Konofagou and J. Ophir, "A new elastographic method for estimation and imaging of lateral displacements, lateral strains, corrected axial strains and Poisson's ratios in tissues," *Ultrasound Med. Biol.*, vol. 24, no. 8, pp. 1183–1199, 1998.
[31] F. Viola and W. F. Walker, "A spline-based algorithm for continuous time-delay estimation using sampled data," *IEEE Trans. Ultrason., Ferroelectr., Freq. Control*, vol. 52, no. 1, pp. 80–93, Jan. 2005.
[32] Z. Liu, C. Huang, and J. Luo, "A systematic investigation of lateral estimation using various interpolation approaches in conventional ultrasound imaging," *IEEE Trans. Ultrason., Ferroelectr., Freq. Control*, vol. 64, no. 8, pp. 1149–1160, Aug. 2017.
[33] W. Choi, M. Kim, J. HakLee, J. Kim, and J. BeomRa, "Deep CNN-based ultrasound super-resolution for high-speed high-resolution B-mode imaging," in *Proc. IEEE Int. Ultrason. Symp. (IUS)*, Oct. 2018, pp. 1–4.
[34] S. Ioffe and C. Szegedy, "Batch normalization: Accelerating deep network training by reducing internal covariate shift," in *Proc. Int. Conf. Mach. Learn.*, vol. 37, Jul. 2015, pp. 448–456.
[35] K. He, X. Zhang, S. Ren, and J. Sun, "Delving deep into rectifiers: Surpassing human-level performance on ImageNet classification," in *Proc. IEEE Int. Conf. Comput. Vis. (ICCV)*, Dec. 2015, pp. 1026–1034.
[36] K. He, X. Zhang, S. Ren, and J. Sun, "Deep residual learning for image recognition," in *Proc. IEEE Conf. Comput. Vis. Pattern Recognit. (CVPR)*, Jun. 2016, pp. 770–778.
[37] J. Jiang and T. J. Hall, "A coupled subsample displacement estimation method for ultrasound-based strain elastography," *Phys. Med. Biol.*, vol. 60, no. 21, pp. 8347–8364, Nov. 2015.
[38] Y. Wang, E. Helminen, and J. Jiang, "Building a virtual simulation platform for quasistatic breast ultrasound elastography using open source software: A preliminary investigation," *Med. Phys.*, vol. 42, no. 9, pp. 5453–5466, Aug. 2015.
[39] Y. Wang, B. Peng, and J. Jiang, "Building an open-source simulation platform of acoustic radiation force-based breast elastography," *Phys. Med. Biol.*, vol. 62, no. 5, pp. 1949–1968, Mar. 2017.
[40] J. Luo, K. Ying, and J. Bai, "Savitzky–Golay smoothing and differentiation filter for even number data," *Signal Process.*, vol. 85, no. 7, pp. 1429–1434, 2005.
[41] X. Song, B. W. Pogue, S. Jiang, M. M. Doyley, H. Dehghani, T. D. Tosteson, and K. D. Paulsen, "Automated region detection based on the contrast-to-noise ratio in near-infrared tomography," *Appl. Opt.*, vol. 43, no. 5, p. 1053, Feb. 2004.
[42] T. Varghese, "Performance optimization in elastography: Multicompression with temporal stretching," *Ultrason. Imag.*, vol. 18, no. 3, pp. 193–214, Jul. 1996.
[43] H. Du, J. Liu, C. Pellot-Barakat, and M.-F. Insana, "Optimizing multi-compression approaches to elasticity imaging," *IEEE Trans. Ultrason., Ferroelectr., Freq. Control*, vol. 53, no. 1, pp. 90–99, Jan. 2006.
[44] R. Keys, "Cubic convolution interpolation for digital image processing," *IEEE Trans. Acoust., Speech, Signal Process.*, vol. 29, no. 6, pp. 1153–1160, Dec. 1981.
[45] L. Ding, H. Zhang, J. Xiao, B. Li, S. Lu, and M. Norouzifard, "An improved image mixed noise removal algorithm based on super-resolution algorithm and CNN," *Neural Comput. Appl.*, vol. 31, no. S1, pp. 325–336, Jan. 2019.
[46] C. Dong, C. C. Loy, K. He, and X. Tang, "Image super-resolution using deep convolutional networks," *IEEE Trans. Pattern Anal. Mach. Intell.*, vol. 38, no. 2, pp. 295–307, Feb. 2016.
[47] J. Jiang and T. J. Hall, "A parallelizable real-time motion tracking algorithm with applications to ultrasonic strain imaging," *Phys. Med. Biol.*, vol. 52, pp. 3773–3790, 2007.
[48] H. Rivaz, E. Boctor, P. Foroughi, R. Zellars, G. Fichtinger, and G. Hager, "Ultrasound elastography: A dynamic programming approach," *IEEE Trans. Med. Imag.*, vol. 27, no. 10, pp. 1373–1377, Oct. 2008.
[49] J. Jiang and T. J. Hall, "A generalized speckle tracking algorithm for ultrasonic strain imaging using dynamic programming," *Ultrasound Med. Biol.*, vol. 35, no. 11, pp. 1863–1879, Nov. 2009.
[50] H. S. Hashemi and H. Rivaz, "Global time-delay estimation in ultrasound elastography," *IEEE Trans. Ultrason., Ferroelectr., Freq. Control*, vol. 64, no. 10, pp. 1625–1636, Oct. 2017.
[51] M. Ashikuzzaman, C. J. Gauthier, and H. Rivaz, "Global ultrasound elastography in spatial and temporal domains," *IEEE Trans. Ultrason., Ferroelectr., Freq. Control*, vol. 66, no. 5, pp. 876–887, May 2019.
[52] F. Yeung, S. F. Levinson, D. Fu, and K. J. Parker, "Feature-adaptive motion tracking of ultrasound image sequences using a deformable mesh," *IEEE Trans. Med. Imag.*, vol. 17, no. 6, pp. 945–956, 1998.
[53] Y. Zhu, T. J. Hall, and J. Jiang, "A finite-element approach for young's modulus reconstruction," *IEEE Trans. Med. Imag.*, vol. 22, no. 7, pp. 890–901, Jul. 2003.

[54] J. Jiang and T. J. Hall, "A fast hybrid algorithm combining regularized motion tracking and predictive search for reducing the occurrence of large displacement errors," *IEEE Trans. Ultrason., Ferroelectr., Freq. Control*, vol. 58, no. 4, pp. 730–736, Apr. 2011.
[55] S. Goenezen, J.-F. Dord, Z. Sink, P. E. Barbone, J. Jiang, T. J. Hall, and A. A. Oberai, "Linear and nonlinear elastic modulus imaging: An application to breast cancer diagnosis," *IEEE Trans. Med. Imag.*, vol. 31, no. 8, pp. 1628–1637, Aug. 2012.
[56] T. J. Hall, A. A. Oberait, P. E. Barbone, A. M. Sommer, N. H. Gokhale, S. Goenezent, and J. Jiang, "Elastic nonlinearity imaging," in *Proc. Annu. Int. Conf. IEEE Eng. Med. Biol. Soc.*, Sep. 2009, pp. 1967–1970.

LIANHAI HE received the B.E. degree in software engineering from Southwest Petroleum University (SWPU), China, in 2017, where she is currently pursuing the Master of Science degree in computer engineering. Her research interests include medical image analysis and deep learning.

BO PENG received the B.E. degree in computer science from Southwest Petroleum University (SWPU), China, in 2003, and the M.S. and Ph.D. degrees in computer science from Sichuan University, China, in 2007 and 2014, respectively. He joined SWPU as a Lecturer, in 2007, where he is currently an Associate Professor of computer science. Under an Oversea Fellowship funded by the Chinese Oversea Scholarship Council, he visited Michigan Technological University as a Postdoctoral Researcher, from 2015 to 2017. His research interests include ultrasound elastography, GPU computation, medical image analysis, and deep learning.

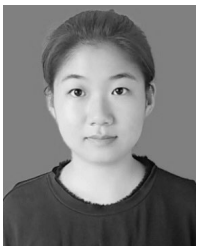

TIANLAN YANG received the B.E. degree in software engineering from Southwest Petroleum University (SWPU), China, in 2017, where she is currently pursuing the Master of Science degree in computer engineering. Her research interest includes ultrasound speckle tracking.

JINGFENG JIANG received the B.S. and M.S. degrees in structural engineering from Zhejiang University, China, in 1995 and 1998, respectively, and the M.S. degree in computer science (image analysis) and the Ph.D. degree in civil engineering (computational mechanics) from the University of Kansas, in 2002 and 2003, respectively.

He was with the Department of Medical Physics, University of Wisconsin–Madison, from 2003 to 2012, first as a Postdoctoral Associate and then as a Research Scientist. He is currently an Associate Professor of biomedical engineering with Michigan Technological University, Houghton, MI, USA. He also holds affiliated/visiting appointments at the University of Wisconsin, Mayo Clinics, and SWPU. His overall research interests stride the borders among imaging, biology, and computational sciences. At the University of Wisconsin, he mainly worked on algorithm developments for ultrasound elastography. More recently, he has expanded his research into advanced open-source elastography simulations (https://github.com/jjiang-mtu/virtual-breast-project), cardiovascular flow analytics and medical image analysis, and machine learning and uncertainty quantification for computational biomechanics.